Comparative analysis of electron–phonon relaxation in a semiconducting carbon nanotube and a PbSe quantum dot*

Bradley F. Habenicht, Svetlana V. Kilina, and Oleg V. Prezhdo‡

Department of Chemistry, University of Washington, Seattle, WA 98125-1700, USA

Abstract: The key features of the phonon-induced relaxation of electronic excitations in the (7,0) zig-zag carbon nanotube (CNT) and the $Pb_{16}Se_{16}$ quantum dot (QD) are contrasted using a time-domain ab initio density functional theory (DFT) simulation. Upon excitation from the valence to the conduction band (CB), the electrons and holes nonradiatively decay to the band-edge in both materials. The paper compares the electronic structure, optical spectra, important phonon modes, and decay channels in the CNT and QD. The relaxation is faster in the CNT than in the QD. In the PbSe QD, the electronic energy decays by coupling to low-frequency acoustic modes. The decay is nonexponential, in agreement with non-Lorentzian line-shapes observed in optical experiments. In contrast to the QD, the excitation decay in the CNT occurs primarily via high-frequency optical modes. Even though the holes have a higher density of states (DOS), they relax more slowly than the electrons, due to better coupling to low-frequency vibrations. Further, the expected phonon bottleneck is not observed in the QD, as rationalized by a high density of optically dark states. The same argument applies to the CNT. The computed results agree well with experimentally measured ultrafast relaxation time-scales and provide a unique atomistic picture of the electron–phonon relaxation processes.

Keywords: carbon nanotubes; quantum dots; electron–phonon interaction; time-domain density functional theory; nonadiabatic molecular dynamics; time-resolved spectroscopy; non-radiative decay.

INTRODUCTION

The ability to manipulate fundamental characteristics of a system merely by altering its physical attributes holds huge promise. Two nanostructures receiving massive attention in this arena are quantum dots (QDs) and carbon nanotubes (CNTs). In QDs, also known as artificial atoms, changes in the size, shape, or topology of the nanostructure determine its unique properties [1]. The electronic structure of a CNT is dictated by its diameter, length, and chiral angle [2]. The tuneability of the properties of these low-dimensional structures has led to a wide range of applications. The new types of physical processes available in QDs motivate their use in spintronics [3] and quantum computing [4]. QDs have been incorporated into photovoltaic [5,6] devices, lasers [7], field-effect transistors [8], and biological sensors. The remarkable structural, mechanical, and electronic properties of CNTs [2] have suggested a variety of applications including nanoscale logic gates [10], quantum wires [11], and field-effect transis-

---

tors [12]. Further, new types of nanoscale graphitic systems are being developed 13–16]. As synthesis of these nanostructures becomes more advanced and the realization of applications moves closer, knowledge of the details of the material's response to optical stimulation is becoming ever more important. The excitation, charge, and phonon dynamics are intimately intertwined and evolve over a range of time-scales and mechanisms.

The nonradiative relaxation of electrons and holes in QDs and CNTs is the focus of many experimental [5–7,17–24] and theoretical [17,25–28] efforts, as it may have a profound effect on a variety of applications. For instance, the charge–phonon interaction determines conductivity and energy loss in CNT wires [11] and field-effect transistors [12], and the electron–phonon relaxation rates determine the efficiency of QD-based lasers [7] and photovoltaic devices [5,6]. Further, detailed information on electron and hole relaxation is pivotal to such applications as CNT logic gates [10] and optical switches [29]. QD application to quantum information processing [3,4] is limited by the phonon-induced dephasing of electrons [25] and spin [20]. Clearly, insight into the charge–phonon interaction in these nanomaterials is extremely important.

CNTs have been extensively studied with time-resolved optical experiments [21–24], producing varying and controversial results. Differences in experimental techniques (i.e., sample preparation, excitation energy, or light intensity) have produced time-scales ranging from less than 100 fs [21,22] to hundreds of fs [23] to more than a picosecond [24] for intraband relaxation. The electron-hole recombination takes at least an order of magnitude longer than the intraband relaxation. Isolated CNTs relax slower than other samples, such as CNT bundles and CNTs incorporated in polymer matrices. The participation of both low-frequency radial-breathing modes (RBMs) and high-frequency longitudinal optical (LO) G-phonons in the charge carrier relaxation has been detected [21,30,31]. A thorough understanding of the experimental data requires time-domain modeling of the observed results at the atomic level.

Optical studies of QDs have hardly been less intensive or thorough [5,6,17–20]. Among the semiconducting QDs studied recently, lead salts, particularly PbS and PbSe, have shown intriguing electronic and transport properties [32,33]. These lead salts have similar effective masses for their electrons and holes due to nearly symmetric valence bands (VBs) and conduction bands (CBs) [34]. The consequence of this, as well as small effective masses of the electrons and holes, is strong quantum confinement effects [32], which induces quantization of bulk electron bands. This discrete electronic energy spectrum has been predicted to have a large effect on the phonon–charge interaction. A phonon bottleneck is expected to greatly increase relaxation times in these QDs due to a mismatch between the energy available from the normal modes and the energy-gap between the electronic states [5]. This phonon bottleneck coupled with low rates of Auger-type cooling due to the symmetric VB and CB is thought to favor carrier multiplication in PbSe and PbS QDs. Time-resolved experiments have observed very high quantum yields [6] via the formation of multiple electron-hole pairs per absorbed photon. Further studies showed ultrafast charge–phonon relaxation [19,35], invalidating the phonon bottleneck theory in PbS and PbSe QDs and postulating that the bottleneck was not necessary for efficient carrier multiplication. Carrier multiplication has great potential for increasing the efficiency of QD photovoltaic cells, as energy normally lost to phonons is instead transferred to another electron-hole pair [5]. Understanding the details of its mechanism and that of the other competing decay channels requires further investigation. Most current theoretical approaches focus on the QD structure and spectra [17,25,36,37], however, real-time simulations of the charge–phonon relaxation are required to elucidate many of the fine details.

The current work analyzes the results of the time-domain ab initio simulations in order to compare and contrast the phonon-mediated electron and hole relaxation dynamics in a CNT and a QD. The simulated dynamics agree with the experimental time-scales and expose a number of surprising aspects of the relaxation processes. The analysis establishes that the electron and hole relaxation pathways are common to the CNT and QD, however, the electronic states and phonon modes facilitating energy dissipation are different in the two materials. In CNTs, the holes relax more slowly than the electrons and

require a Gaussian and exponential fit to their energy decay, while electrons are well fit by pure exponential. Both electrons and holes couple to the high-frequency C–C stretching optical modes. However, the electrons couple to the optical modes more strongly than the holes, while the latter can also couple to lower-energy acoustic modes. In QDs, the electron and hole relaxation is nearly symmetric, with no observation of a phonon bottleneck. This is attributed to the relatively high density of states (DOS). Though not all states are optically active, most of them facilitate the phonon-induced relaxation. The slight asymmetry in the electron and hole band structure is sufficient to allow symmetry-forbidden transitions that can be detected in the optical spectra. Both electrons and holes in the QD couple primarily to low-frequency acoustic modes. The relaxation proceeds through multiple states at intermediate energies and is notably nonexponential, agreeing with the non-Lorentzian spectral line-shapes [17]. The holes decay slightly faster than the electrons due to their higher DOS. The difference in the hole and electron relaxation times is insignificant, such that Auger energy exchange between the charge carriers cannot speed up the overall relaxation. This is in contrast, for instance, to CdSe QDs, in which holes relax significantly faster than electrons, and electrons are able to lose energy through holes by Auger processes [18]. The relaxation is several times slower than the observed carrier multiplication time [5,6].

The paper is constructed as follows. The next section presents the two essential and closely intertwined theories that form the foundation for the atomistic simulation of the excitation dynamics in the nanoscale materials. These are the time-dependent density functional theory (TDDFT) and the nonadiabatic molecular dynamics (NAMD), which determine the evolution of the electronic and vibrational degrees of freedom, respectively. Following the simulation details, the results section comprises three subsections, focusing on the electronic structure and spectra of the CNT and QD, the phonon modes that couple to the electronic subsystem, and the details of the electron–phonon relaxation dynamics. The paper concludes with a discussion and summary of the key results, emphasizing the similarities and differences of the two materials.

THEORY

The time-domain atomistic ab initio simulation of the charge–phonon relaxation dynamics was made possible by the recent implementation [38] of trajectory surface hopping (TSH) [39–41] within time-dependent Kohn–Sham (KS) theory [42–44]. TSH is a fully atomistic NAMD approach and is one of the most common NAMD schemes [38,45–47]. It satisfies detailed balance [41] and can be viewed as a quantum master equation for electron dynamics, in which the state-to-state transition rates depend on time via coupling to explicit phonon dynamics.

Time-dependent density functional theory

In the KS representation [42–44] of TDDFT, the electron density is written as

$$\rho(x,t) = \sum_{p=1}^{N_e} \left| \varphi_p(x,t) \right|^2 \tag{1}$$

N_e is the number of electrons in the system, and $\varphi_p(x, t)$ represents the single-electron KS orbitals. Application of the TD variational principle to the KS energy determines the evolution of the coefficients, $\varphi_p(x, t)$.

$$E\{\varphi_p\} = \sum_{p=1}^{N_e} \langle \varphi_p | K | \varphi_p \rangle + \sum_{p=1}^{N_e} \langle \varphi_p | V | \varphi_p \rangle + \frac{e^2}{2} \int\int \frac{p(x',t)\rho(x,t)}{|x-x'|} d^3x d^3x' + E_{xc}\{\rho\} \tag{2}$$

The right-hand side of eq. 2 gives the kinetic energy of noninteracting electrons, the electron-nuclear attraction, the Coulomb repulsion of the density $\rho(x, t)$, and the exchange-correlation energy functional that accounts for the residual many-body interactions. Application of the variational principle leads to a system of single-particle equations [42–44]

$$i\hbar \frac{\partial \varphi_p(x,t)}{\partial t} = H\left[\varphi(x,t)\right]\varphi_p(x,t), \; p = 1,...,N_e \tag{3}$$

where the Hamiltonian H depends on the KS orbitals. This simulation utilizes the generalized gradient approximation (GGA) [48], where E_{xc} depends on both the density and its gradient, and the Hamiltonian is written as

$$H = -\frac{\hbar}{2m_e}\nabla^2 + V_N(x) + e^2 \int \frac{\rho(x')}{|x-x'|}d^3x' + V_{xc}\{\rho, \nabla\rho\} \tag{4}$$

Expanding the time-dependent $\varphi_p(x, t)$ in the adiabatic KS orbitals $\varphi_k(x; R)$

$$\varphi_p(x,t) = \sum_k^{N_e} c_{pk}(t)\left|\bar{\varphi}_k(x;R)\right\rangle \tag{5}$$

the TDDFT eq. 3 transforms into an equation of motion for the coefficients

$$i\hbar \frac{\partial}{\partial t}c_{pk}(t) = \sum_m^{N_e} c_{pm}(t)\left(\varepsilon_m\delta_{km} + \mathbf{d}_{km}\cdot\dot{\mathbf{R}}\right) \tag{6}$$

The NA coupling

$$\mathbf{d}_{km}\cdot\dot{\mathbf{R}} = -i\hbar\left\langle\bar{\varphi}_k(x;R)\left|\nabla_{\mathbf{R}}\right|\bar{\varphi}_m(x;R)\right\rangle\cdot\dot{\mathbf{R}} = -i\hbar\left\langle\tilde{\varphi}_k\left|\frac{\partial}{\partial t}\right|\tilde{\varphi}_m\right\rangle \tag{7}$$

arises from the dependence of the adiabatic KS orbitals on the nuclear trajectory, and is computed most easily from the right-hand side of eq. 7 [40].

The time-dependence in TDDFT for electron-nuclear dynamics is due to ionic motion, making $V_N(x) \equiv V_N[x; \mathbf{R}(t)]$ dependent on time through the nuclear trajectory $\mathbf{R}(t)$. The evolution of $\mathbf{R}(t)$ constitutes the quantum back-reaction problem. TSH uses a stochastic element that creates both classical trajectory branching [39] and detailed balance [41]. The former mimics the ability of quantum mechanical wave-packets to split and evolve in correlation with different electronic states, an area of intense interest [49]. The latter is essential for relaxation and leads to thermodynamic equilibrium.

Fewest switches surface hopping in the KOHN–SHAM representation

TSH propagates the electronic subsystem using a set of basis states. The classical nuclear trajectories correlate with these states via hops between states. It has been shown that the adiabatic basis is preferable for TSH [39–41]. The adiabatic states are eigenstates of the Hamiltonian eq. 4. While the adiabatic forces for ground- and excited-electronic states as well as the NA coupling between them can be calculated in TDDFT [42–44], the NA coupling between excited electronic states has not been rigorously defined yet. TSH was performed in the zero[th] order adiabatic basis in ref. [38], using Slater determinants formed of adiabatic KS orbitals. In the present study, there is a further approximation by going from the many-particle to the single-particle representation. TSH is performed in the basis of the single-particle adiabatic KS orbitals. As the electronic structure of QDs is well represented by the inde-

pendent electron and hole picture, it is advantageous to use the simplicity of the single-particle picture. Quantum confinement effects in small-diameter QDs ensure that the electron and hole kinetic energies dominate the electrostatic interaction, avoiding strongly bound excitons. As a result, the basic effective mass theory provides a good description of the QD electronic structure, validating our simulation. Quantum confinement effects are particularly strong in PbSe and are evident in QDs whose size is comparable to or smaller than the PbSe exciton localization length $d = 46$ nm [32].

In CNTs, optical excitations can lead to exciton formation due to its quasi-1D structure. Excitons have been shown to be fairly strongly bound [26,50]. However, intraband relaxation occurs rapidly in CNTs, and there is evidence that exciton formation does not occur until the hot electrons and holes have cooled [22]. Further, electron-hole correlations are implicitly included in TDDFT, which is manifest in the asymmetric DOS of a CNT. Thus, in the time-scale of our simulation, the single-particle representation should be valid for CNTs as well.

TSH prescribes a probability for transitions or "hopping" between electronic states. The probability is explicitly time-dependent as the motions of the ions induce coupling between electronic states. In the fewest switches TSH [39], the probability to hop within the time interval dt between states m and n is defined as

$$d\mathrm{P}_{mn} = \frac{b_{mn}}{a_{mm}} \, dt \tag{8}$$

where

$$b_{mn} = -2\,\mathrm{Re}\left(a_{mn}^* \mathbf{d}_{mn} \cdot \dot{\mathbf{R}}\right); \quad a_{mn} = c_{mn} c_{mn}^* \tag{9}$$

Here, c_m and c_n are the coefficients evolving according to eq. 6. The transition probabilities directly depend on the NA coupling $\mathbf{d}_{mn} \cdot \dot{\mathbf{R}}$ defined in eq. 7. If the calculated probability is negative, the hop is denied. Physically, this feature minimizes the number of hops by restricting transitions from state m to state n to events where the electronic occupation of state m decreases and the occupation of state n increases. To conserve the total electron-nuclear energy after a hop and include back-reaction from the electronic system to the ionic, the nuclear velocities are rescaled [39], along the direction of the electronic component of the NA coupling $\mathbf{d}_{mn}$. In order to avoid unphysical transitions predicted by eq. 8, all NA transitions to higher-energy electronic states are checked against the kinetic energy available in the nuclear coordinates along the direction of the NA coupling. If the kinetic energy is insufficient to accommodate the increase in the electronic energy, the hop is rejected. The velocity-rescaling and hop-rejection give detailed balance between upward and downward transitions [41].

The current, simplified implementation of TSH assumes that energy exchanged between the electronic and select nuclear degrees of freedom is rapidly distributed among all nuclear modes. Under this assumption, the distribution of energy in the nuclear mode directed along the NA coupling $\mathbf{d}_{mn}$ is Boltzmann at all times. The velocity-rescaling plus hop-rejection is then replaced by multiplying the probability, eq. 8, for transitions upward in energy by the Boltzmann factor. This elimination of the velocity-rescaling gives great computational savings, allowing one to use a predetermined nuclear trajectory to evolve the electronic subsystem.

To summarize, a simplified version of fewest switches TSH is performed in the single-particle TDKS representation, with the hop-rejection replaced by multiplication of the TSH probability upward in energy by the Boltzmann factor. The NA electronic evolution, eq. 6, is evaluated using the ground-state nuclear trajectory. This treatment of the electron and hole relaxation creates a sophisticated version of the quantum master equation with explicitly time-dependent transition probabilities that respond to nuclear evolution and give the correct short- [51,52] and long-time dynamics [39–41].

Simulation details

The VASP [53] DFT package was used to generate the nuclear trajectories, allowing the electronic evolution via TSH in the TDKS basis [38]. The Perdew-Wang GGA [48], Vanderbilt ultrasoft pseudo-potentials [54], periodic boundary conditions, and converged plane-wave basis sets are employed in the simulation.

The structure of the nanotube and QD and the dimension of the simulation cell along the tube are optimized to obtain the minimum energy structure. 8 Å of vacuum is added to the direction perpendicular to the nanotube axis and in all directions of the QD cell to avoid nonphysical interactions. After heating the system to 300 K by repeated velocity rescaling, a 1.5 ps (CNT) or 4 ps (QD) microcanonical trajectory is run in the ground electronic state with a 1 fs time step, and 400 initial conditions are sampled for the relaxation dynamics. The electron evolution is done on a 10^{-3} fs time-scale. The transition dipole moments and oscillator strengths (OSs) for excitations between KS orbitals were computed and used both to generate the optical absorption spectrum and to pick the most optically active excitations for the initial conditions of the NAMD runs.

The (7,0) nanotube is the smallest semiconducting CNT [2]. It is an achiral zig-zag CNT with chiral vector of 0 degrees and has a diameter of 5.5 ~Å. This tube has been chosen to minimize the size of the electronic basis and simulation cell. Constructing the simulation cell from four CNT unit cells and 112 carbon atoms (see Fig. 1a) expands the available phonon spectrum [55].

The QD was constructed on a zinc-blend lattice of 16 atoms of Pb and 16 atoms of Se with bulk Pb–Se bond lengths. It was then relaxed to its lowest energy configuration at zero temperature. This relaxed configuration was heated to 300 K by continuous velocity-rescaling and used for further dynamics calculations. Figure 1d compares the relaxed atomic geometries at zero and at room temperatures with the initial bulk structure. Significant structural deviation of the QD from the bulk was observed even at zero temperature. Temperature-induced fluctuations further distort the dot, but do not cause surface reorganization or bond reconnectivity, Fig. 1d. The diameter of the roughly spherical 32-atom PbSe nanocrystal is about 1 nm. Since PbSe is strongly ionic, its electronic properties are not strongly influenced by the surface structure [32], and the surface was not passivated, creating substantial computational savings.
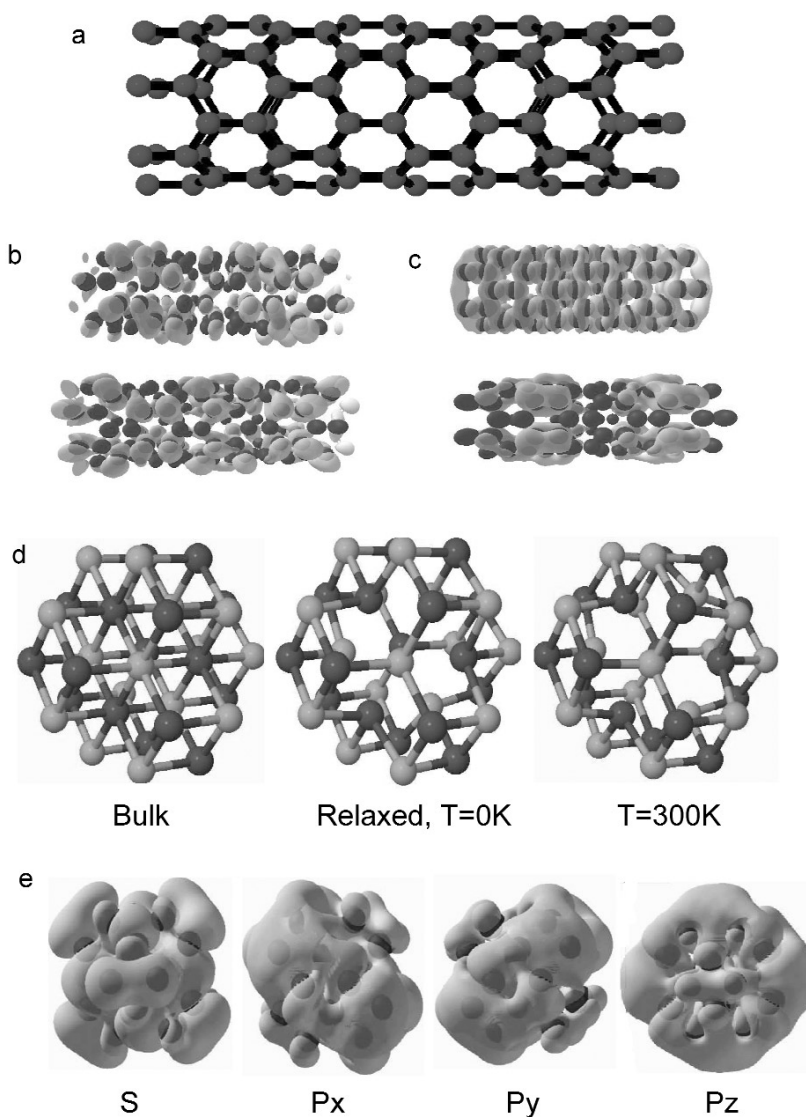
Fig. 1 Schematic of the nanostructures used in the simulation and partial charge densities of important states. (a) The 112-atom simulation cell of the (7,0) CNT is comprised of 4 units cells. Partial charge densities of the important initial states for (b) electrons and (c) holes. The relaxation of the 32-atom PbSe QD from bulk geometry at 0 and 300 K is shown in (d), Pb atoms are black and Se atoms are gray. In (e), the charge densities of the lowest electronic states are shown. The states are classified by their overall symmetry.

RESULTS

The implementation of time-domain ab initio simulation of charge–phonon processes allows for the detailed study of the relaxation dynamics that was not previously possible. Traditional DFT studies provided the optimized structures and optical spectrum of the CNT and QD, respectively. Our NAMD approach directly probes the relaxation mechanisms, identifies the phonon modes that couple the adiabatic states, and allows for direct comparison to time-resolved experimental data.

Electronic structure and optical spectra

The electronic DOS of the CNT and QD are presented in Fig. 2. The CNT has an asymmetric DOS, as opposed to the symmetric DOS of the tight-binding model [2]. Van Hove singularities (vHS), due to quantum confinement around the circumference of the nanotube are visible both above and below the Fermi energy. Our simulation models ultrafast spectroscopic experiments where an electron is excited from the second vHS below the Fermi level to the second vHS above the Fermi level (2'-2). These transitions are strongly optically active and are modeled by computing the OS. Over a third of all excitations occur between two pairs of electron and hole states. The partial charge densities of these important states are shown in Figs. 1b and 1c. Note the much smoother density of the hole states (Fig. 1c). The relaxation of the electron and hole is then monitored as it moves through the DOS to the band-edge. The calculated optical spectrum of the (7,0) CNT is shown in Fig. 3a. The three large peaks correspond to transitions between vHS in the VB to vHS in the CB as labeled. The electron-hole correlation effects included in DFT, together with the high amount of strain due to the narrow diameter of this nanotube, allow for large OS of the 1'-2 and 3'-2 transitions.

The partial charge densities of the first four electronic states above the band-edge of the PbSe QD are shown in Fig. 1e. The symmetries of these states are roughly S- and P-type, though strongly modified by the atomic structure. This agrees with effective mass theory [36,37], which represents the electron and hole wave-functions as products of Bloch functions that vary on the atomistic level. It also includes S-, P-, D-, etc. envelope functions that encompass the whole QD and are eigenstates of a particle in a spherical well. The S- and P-symmetries are less pronounced in the corresponding hole states at the edge of the VB.

The variation of the DOS of the PbSe cluster over a 3.5 ps time interval is presented in Fig. 2b. The calculated average energy-gap of the 1 nm QD is 1.4 eV, which follows the expected trend of increasing band-gap with decreasing QD diameter. The calculated gap exceeds the 1.25 eV gap observed experimentally for a 1.4 nm QD [19]. The gap is likely underestimated, as is common in DFT. The electronic structure and optical properties of bulk lead salts computed with a similar approach agree well with the experimental results [56].

The shape of the calculated DOS and the OS spectrum, Figs. 2b and 3b, follow the experimental data [19,34,35] and the ab initio tight-binding results [57]. The three main peaks on each side of the gap can be attributed to the expected transitions between the S_e (S_h), P_e (P_h), and D_e (D_h) levels of electrons (holes). The separation of the S-state from the main manifold is more pronounced with the electrons than the holes, the latter having a denser distribution of states. The difference in the electron and hole DOS for PbSe QDs is not nearly as pronounced as in other QDs, for instance, CdSe QDs [17,18]. The arrows in Fig. 2b indicate the energies of electron and hole excitations, which are set to match three times the QD energy-gap in correspondence with experiment [6]. The arrow in Fig. 3b indicates the initial excited states, which were chosen based on the transition dipole moment for a given nuclear configuration. The excitation energy was chosen to match experiment at three times the band-gap. The similarity in the electron and hole state structure results in selection rules that favor symmetric photoexcitations across the gap [32].

Figure 3b shows the calculated optical absorption spectrum of the PbSe QD. The strongest peaks in the spectrum correspond to symmetric transitions (e.g., S–S and P–P), as expected from the selection rules. The slight asymmetry in the electron and hole DOS, Fig. 2b, is sufficient to allow asymmetric transitions (e.g., S–P) that create optical bands. The asymmetric transitions can be less pronounced in larger clusters, since the anisotropy of the small $Pb_{16}Se_{16}$ cluster shape and its deviation from the bulk geometry (Fig. 1d), can have a strong effect on the broken selection rules.
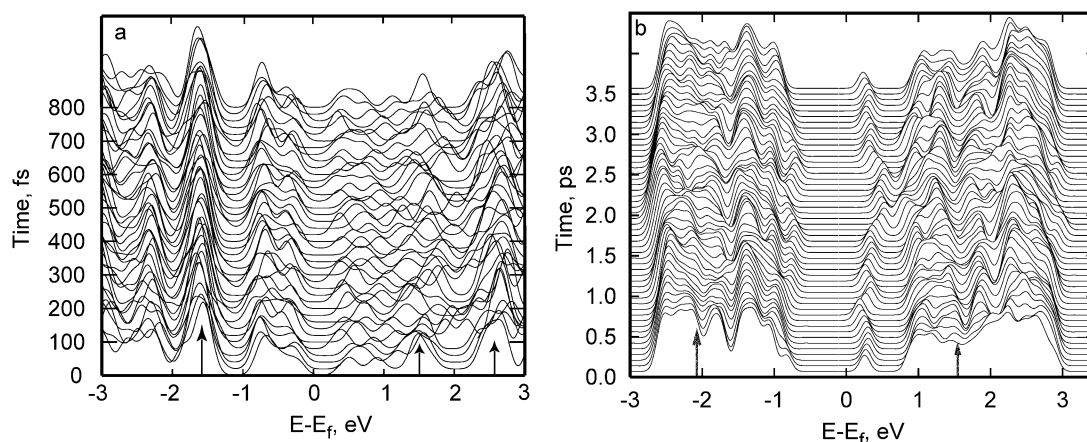
Fig. 2 Evolution of the DOS with time for (a) CNT and (b) QD. The arrows show the energies of the initial states, chosen to model experiment and representing the most optically active transitions. In both the QD and CNT, the holes at negative energies have a denser manifold of states than the electrons at positive energies.
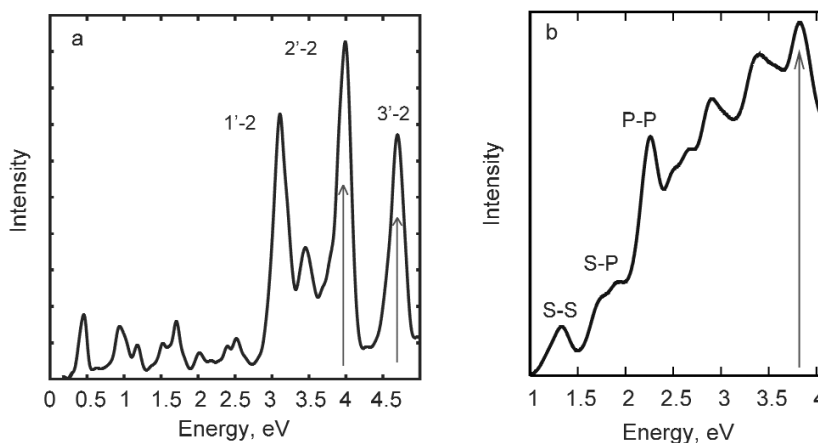

Fig. 3 Calculated absorption spectra of (a) CNT and (b) QD. In both systems, the strongest transitions are those between states of the same symmetry. Due to the small diameters of the CNT and QD, however, transitions typically forbidden by symmetry have substantial OS.

Phonon modes

The difference in the dimensionality, bonding topology, and atomic masses of CNTs and QDs lead to very different vibrational spectra of the nanostructures, Fig. 4. Figure 4a shows the Fourier transform (FT) of the energy fluctuations of the two most important initial CNT electron and hole states. The NA coupling is directly proportional to the second derivative of the energy along the nuclear trajectory [58]. Therefore, the vibrational modes that regulate the oscillations in the energy levels create the largest coupling.

In CNTs, two modes generally domintate the vibrations: the low-frequency acoustic RBM and the high-frequency optical G-mode. The RBM corresponds to the atoms in the CNT collectively moving inwards and outwards and is found near 300 cm^{-1}. The G-mode represents C–C stretches and is around 1600 cm^{-1}. From the calculated vibrational structure, the CB states couple strongly to higher-energy modes, particularly the G-mode. The VB states also couple to high-energy modes, however, not as
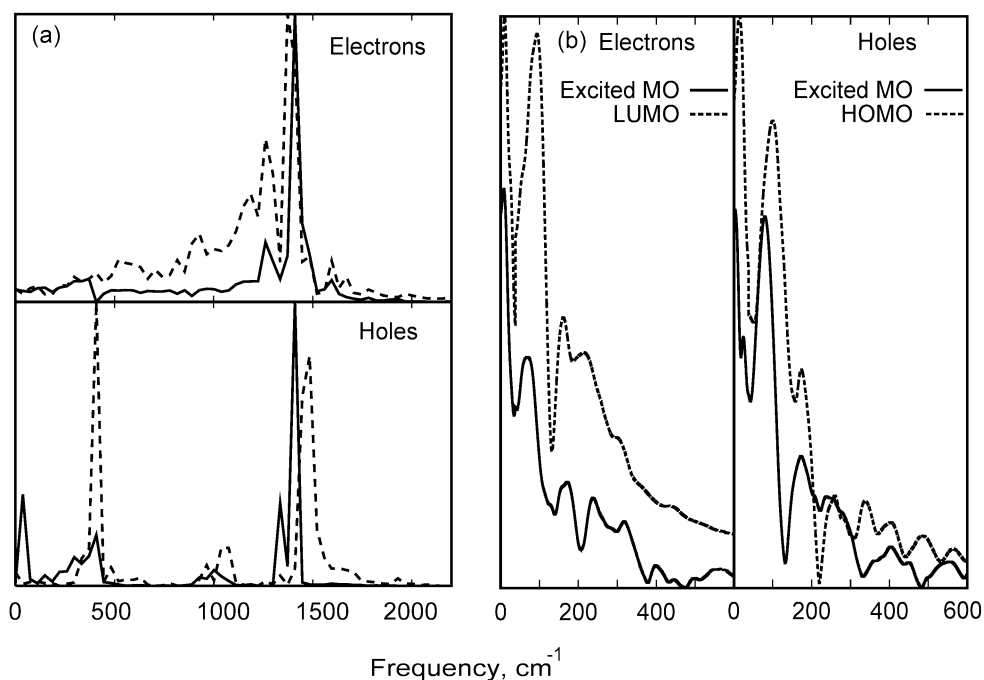
Fig. 4 Spectra of the phonon modes that couple to the electronic subsystem in (a) CNT and (b) QD. For the CNT, the electrons couple primarily to high-energy optical phonons. Holes couple to the optical phonons as well, however, they also strongly couple to the lower-energy acoustic modes. States shown are the most common initial VB and CB states. For the QD, both electrons and holes couple more strongly to the acoustic phonons around 100 cm^{-1} and below. Electrons couple slight better to the higher-energy optical phonons near 200 cm^{-1}.

strongly, and they couple to the lower-energy acoustic phonons such as the RBM. This stronger coupling to the RBM can be rationalized by the energies of the states. The VB (hole) states are lower-energy and thus have fewer nodes. These "smoother" charge densities are then more strongly influenced by the lower-energy acoustic modes, which also have fewer nodes than the optical modes. The CB states are higher in energy, have more nodes, and couple more strongly to the optical phonons that also have more nodes.

   Figure 4b shows the phonon modes that influence relaxation in PbSe QDs. The figure depicts the FTs of the energies of highest occupied and lowest unoccupied molecular orbitals (HOMO/LUMO) and the most optically active electron and hole states. In a QD, the vibrational spectrum has contributions from spheroidal acoustic phonons and LO phonons. Our simulation agrees well with experiment [32] that the spheroidal acoustic phonons with frequencies around 100 cm^{-1} and below dominate the electron and hole dynamics. The LO phonons around 200 cm^{-1} also effect the energy fluctuations, however with much smaller amplitude. The acoustic modes modulate the QD size, which has a profound effect on the state energies and wave-functions. The optical phonons are local stretching modes, and these atomic displacements tend to average out over the whole QD, creating smaller NA coupling.

   In contrast to the CNT, the amplitudes and frequencies of the active phonon modes are quite similar for both the electron and holes of the QD. This suggests that the charge relaxation dynamics should be similar for both electrons and holes. The electrons have a slightly broader influence spectrum with more high-frequency contributions than the holes. As the electron states represent higher-energy KS orbitals, which contain more nodes, they better couple with the higher-frequency LO vibrations.

Phonon-induced electronic relaxation

Relaxation of the electrons and holes through the DOS of the CNT and QD are shown in Figs. 5a and 5b, respectively. The decay was fit using a Gaussian plus exponential equation

$$E(t) = \left(E_i - E_f\right)\left\{A_G \exp\left[-0.5\left(t / \tau_G\right)^2\right] + \left(1 - A_G\right)\exp\left[-t / \tau_{exp}\right]\right\} + E_f \qquad (10)$$

and the results are shown in Tables 1 and 2. Surprisingly, for the CNT, the holes relax slower than the electrons despite the greater DOS for the holes (Fig. 5a). As shown, the electron energy decay can be fit well with a pure exponential, while the hole decay has a much stronger Gaussian component (Table 1). The data is in good agreement with experimental time-scales [23], especially considering our simulation is in vacuum and experiments involve interactions with outside environments [59], especially complex solvation [60] or incorporation into polymer matrices. Interaction with solvent can broaden spectral lines and provide or enhance vibrational decay channels [61]. The Gaussian relaxation observed with holes at short times is associated with coherent quantum dynamics [51,62] that results in delocalization of holes over their dense state manifold. The lower density of electronic states restricts the amplitude of the coherent dynamics. Holes starting closer to the Fermi energy have smaller DOS and relax more slowly, in agreement with the experimental data [23]. This Gaussian and exponential decay of the holes is rationalized by its coupling to both the RBM and G-mode (Fig. 4a). The electron's single component decay is due to its lack of coupling to the RBM or other lower-frequency acoustic modes.
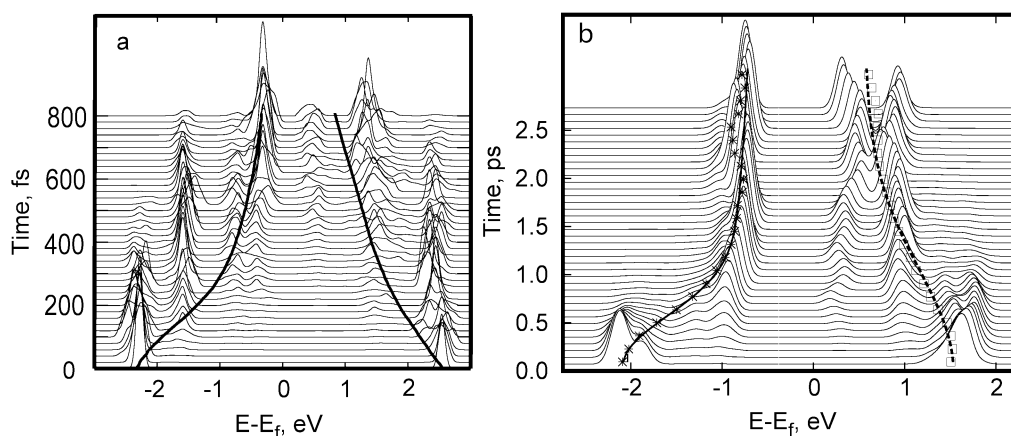
Fig. 5 Evolution of the electrons (positive energies) and holes (negative energies) with time in (a) (7,0) CNT and (b) PbSe QD. The initial Gaussian component of the holes in the CNT is visible as is the pure exponential decay of the electrons. In the QD, the electrons and holes relax nearly symmetrically until they are near the band-edge. The electrons take slightly longer due to a smaller DOS. The larger splitting between the S- and P-symmetry states in the CB keeps the electrons from relaxing to the LUMO in the time-scale of this simulation.

Table 1 Parameters of the Gaussian plus
exponential fits, eq. 10, to the average electron
and hole energy decays in the CNT, Fig. 4a.

	τ_G, ps	τ_{exp}, ps	A_G
Electrons (squares)	0.20	0.32	0.20
Electrons (squares)[a]	–	0.38	0.00
Holes (circles)	0.28	0.71	0.65
Holes (pluses)	0.41	0.94	0.55

[a]The purely exponential fit line (not shown in Fig. 4a) is
very close to the Gaussian plus exponential fit.

Table 2 Parameters of the Gaussian plus
exponential fit, eq. 10, to the average electron and
hole energies in the QD, Fig. 4b.

	τ_G, ps	τ_{exp}, ps	A_G
Holes	0.45	2.7	0.70
Electrons	0.80	2.7	0.75

The fit of the energy relaxation of the QD electrons and holes shown in Fig. 5b is not exponential, which agrees with the strongly non-Lorentzian line-shapes observed experimentally [17]. Note that standard master-equation treatments [63] with constant transition rates give exponential relaxation. The nonexponential profile of the energy decay present in the current simulation is due to the explicit time-dependence of the relaxation rates provided by TSH [38–41]. TSH correctly represents the vanishing time-derivative of the quantum mechanical transition probability at zero time, which is manifested in the quantum-Zeno effect [51,52] and gives the Gaussian relaxation component at early times.

This initial Gaussian component of the QD decay accounts for 70 % of the hole and 75 % of the electron relaxation amplitudes. It dominates the exponential portion in both particles. The DOS and active mode frequencies both influence the relaxation rate and profile. The large DOS promotes faster relaxation, while the mode frequencies determine the time-scale at which the phonons are able to interact with the charge carriers. The electrons have a smaller DOS than the holes, but couple slightly better to higher-energy phonons. In this case, however, the DOS is more important, as the holes decay more quickly than the electrons. The calculated Gaussian and exponential components (Table 2) of the charge–phonon relaxation are in good agreement with experiment. The measured results are sub-picosecond to picosecond times, and become faster for smaller QDs [19,35]. The reported results indicate that the phonon bottleneck to the electron and hole relaxation occurs only at the last stages of the simulated relaxation, and even then mostly for the electrons due to the pronounced energy difference between the S- and P-symmetry states. The lack of the bottleneck in the initial relaxation may be rationalized via the relatively dense spacing of the electron and hole states at higher energies. Except for the two lowest-energy states of the CB, the typical spacing between the photoexcited state and its nearest neighbors nearly matches the phonon frequencies.

DISCUSSION AND CONCLUSIONS

The phonon-mediated electron and hole dynamics in the CNT and the QD simulated by ab initio TDDFT provides a unique comparison of the excitation decay in these materials in real time and at the atomistic level of detail. The calculated relaxation time-scales agree with the direct experimental data [19,21–24,35] showing subpicosecond to several picosecond relaxation that becomes faster in smaller QDs and subpicosecond relaxation times in a CNT that depend on the excitation energy. In our simu-

lation of a small dot, the bulk of the relaxation occurs within 0.45–0.8 ps. The minor 2.7 ps component seen once the particle has neared the band-edge is due to the small size of the simulated QD, which creates gaps between the first and second band-edge states, particularly for the electron. The simulated 0.45–0.8 ps relaxation also agrees with the experimental detection of charge carrier multiplication that occurs within 0.25 ps and successfully competes with the relaxation [6]. In CNTs, the electron relaxes to the band-edge exponentially within 200–300 fs, while the hole takes a 300–400 fs Gaussian and a 700–900 fs exponential decay of about equal importance.

The atomistic picture of the PbSe QDs provided by the simulation explains the seemingly contradictory experimental observations of the large line spacing in the optical spectra of QDs and the absence of the phonon bottleneck. The spacing between the state energies nearly matches the phonon frequencies, in contrast to the common belief that the quantum confinement results in strong quantization of electronic energy levels in QDs. The optical absorption spectrum displays discrete bands that may be attributed to S–S, P–P transitions as described in the effective mass theory [36,37], with each band representing multiple excitations between electron and hole states. The optical selection rules, which are clearly defined in the effective mass approach, are also seen in the ab initio calculation, in which most of the states are weakly optically active. The optical selection rules are determined by the x, y, and z light polarization components. The electron-phonon coupling selection rules, however, are much more relaxed. Single or multiple phonons of various symmetries couple nearly all of the electronic states, which facilitates the nonradiative relaxation. While not all states are equally optically active, the majority of them take part in the relaxation due to the relaxed electron-phonon selection rules.

The small asymmetry in the DOS and the slight deviation from the bulk geometry is sufficient to break the optical selection rules that require symmetric transitions (e.g., S–S and P–P). The excitations between different symmetry states, such as S–P and P–S, in the VB and CB create additional absorptions in the optical spectrum. These excitations are not as strong as the symmetric excitations, however, they can be detected experimentally. The S–P and P–S transitions occur at different energies owing to the larger energy spacing between the states in the CB. The higher hole DOS provides more relaxation pathways, and the holes relax slightly faster than the electrons to the band-edge. However, since the DOS is only slightly larger and the electrons and holes couple to very similar phonons, the slight difference in the electron and hole relaxation time-scales renders inefficient the hole-assisted Auger relaxation pathway, in which, first, the electron energy is transfered to the hole and, second, the hole rapidly loses its energy. The highly nonexponential profile of simulated energy decay agrees with the strongly non-Lorentzian spectral line-shapes observed experimentally.

The calculated relaxation of the CNT charge carriers support the picture where the photoexcited state scatters into the continuum of hot electron and hole pairs, which relax by phonon emission [22]. The absorption spectra of the CNT is dominated by excitons that arise due to confinement of the wavefunction along the axis of the tube. However, the intermediate bands, which represent states that are delocalized along the length of the nanotube, contribute greatly to the nonradiative relaxation of electrons and holes. These bands provide a channel, through which the charged particles relax to the band-edge. In this sense, the phonon-induced electronic relaxation is similar in both CNT and QD. The relatively few optically active excited states decay through the multitude of dark states, and the wide energy spacing between the optically active states does not create a phonon bottleneck.

The G-type LO phonons with frequencies around 1500 cm^{-1} provide the fastest relaxation pathway for both electrons and holes in the CNT. The G-mode and RBM are most effective in modulating the state energies, thereby creating avoided crossings between the states and promoting the NA transitions that are responsible for the relaxation. The LO phonons dominate both electron and hole relaxation, though the hole relaxation is influenced greatly by its greater DOS and coupling to the RBM. The involvement of RBM in the CNT charge carrier dynamics has been detected by both current/voltage [30] and spectroscopic [21] measurements. The coupling of the electronic system to the LO phonons has been detected in the Raman spectra [31]. The reported ab initio NA dynamics also agree with the

tight-binding electronic structure calculations, in which the electron-phonon scattering was dominated by the RBM and LO phonons in two narrow frequency regions [64].

The relaxation in this simulation occurs through NA charge–phonon interactions. In QDs, charge carriers interact more strongly with acoustic than with optical phonons. This is because the NA coupling is directly related to the second derivative of the energy, and the latter is more sensitive to acoustic modes that modulate the shape and size of the dot and less sensitive to optical modes, whose effect on the energy tends to average out over the multiple bulk semiconductor unit cells that form the QD. In CNTs, the charge carriers interact more strongly with optical phonons. The optical phonons are higher-energy than in QDs, have a greater effect on the energy fluctuations of the bands, and allow larger amounts of electronic energy to be lost to heat. In both QDs and CNTs, electrons interact better with optical modes, as can be rationalized by the better match between the nodal structure of the CB states and optical modes. The lower-energy VB states that support holes have fewer nodes than the CB states that support electrons; similarly, RBMs and other acoustic phonons have fewer nodes than LO phonons. As a result, acoustic phonons couple better to the VB states. The stronger coupling in CNTs to the lower-frequency modes explains why the hole relaxation is slower than the electron relaxation in CNTs, even though holes have a higher DOS. In QDs, however, the VB and CB are more symmetric, thus, the higher DOS for holes is more important. Further, in QDs the energy difference between acoustic and optical phonons is only about 100 cm^{-1}. In CNTs, however, the energy difference is an order of magnitude larger at around 1000 cm^{-1}.

The computational expense limits the simulations to a small 32-atom PbSe QD and a 112-atom, small-diameter CNT. The small QD deviates from the bulk geometry, yet, gives a good representation of larger QDs. The 32-atom cluster preserves the bulk topology and is not an amorphous collection of atoms. Therefore, it belongs to the same type of material as the larger dots. Although the surface relaxation and the shape asymmetry should be less pronounced in larger QDs, the high-state degeneracy of an ideal spherical potential is still lifted in larger dots due to disorder generated by thermally activated phonon modes. The (7,0) CNT does suffer from strain induced by its small diameter. This is shown via a shift in the G-mode from larger-diameter tubes. Still, the general trends in coupling the DOS are preserved in the carbon lattice and should be transferable to larger CNTs.

In summary, the time-domain ab initio simulations generate valuable insights into the properties of these nanostructures. In the CNT, the key observations include the slower, Gaussian, and exponential time-scale hole relaxation and the faster single-component electron dynamics. Despite the smaller-electronic DOS, the electrons relax faster due to the coupling with high-frequency modes. This difference in relaxation between electrons and holes may increase the efficiency of Auger-type relaxation pathways. We further demonstrate that the relaxation rate increases with excitation energy, highlight the importance of the high-frequency LO phonons, and show the substantial contribution of RBM to hole, but not electron relaxation. In QDs, we reconcile the seemingly contradicting observations of wide optical line spacing and no phonon bottleneck to the relaxation, and rationalize why the highly efficient carrier multiplication is possible in PbSe nanocrystals despite the absence of the phonon bottleneck.

REFERENCES

1. J. Jortner, C. N. R. Rao. *Pure Appl. Chem.* **74**, 1491 (2002).
2. R. Saito, G. Dresselhaus, M. S. Dresselhaus. *Physical Properties of Carbon Nanotubes*, Imperial College Press, London (1998).
3. M. Ouyang, D. D. Awschalom. *Science* **301**, 1074 (2003).
4. J. Petta, A. Johnson, J. Taylor, E. Laird, A. Yacoby, M. Lukin, C. Marcus, M. Hanson, A. Gossard. *Science* **309**, 2180 (2005).
5. A. J. Nozik. *Annu. Rev. Phys. Chem.* **52**, 193 (2001).
6. R. D. Schaller, V. I. Klimov. *Phys. Rev. Lett.* **92**, 186601 (2004).

7. V. I. Klimov, A. A. Mikhailovsky, S. Xu, A. Malko, J. A. Hollingsworth, C. A. Leatherdale, H. J. Eisler, M. G. Bawendi. *Science* **290**, 314 (2000).
8. D. Talapin, C. Murray. *Science* **310**, 86 (2005).
9. P. Alivisatos. *Pure Appl. Chem.* **72**, 3 (2000).
10. N. Mason, M. J. Biercuk, C. M. Marcus. *Science* **303**, 655 (2004).
11. S. J. Tans, M. H. Devoret, H. J. Dai, A. Thess, R. E. Smalley, L. J. Geerligs, C. Dekker. *Nature* **386**, 474 (1997).
12. J. A. Misewich, R. Martel, P. Avouris, J. C. Tsang, S. Heinze, J. Tersoff. *Science* **300**, 783 (2003).
13. D. J. Klein, A. T. Balaban. *J. Chem. Inf. Model.* **46**, 307 (2006).
14. A. Kruger, F. Kataoka, M. Ozawa, T. Fujino, Y. Suzuki, A. E. Aleksenskii, A. Y. Vul, E. Osawa. *Carbon* **43**, 1722 (2005).
15. E. D. Eidelman, V. I. Siklitsky, L. V. Sharonova, M. A. Yagovkina, A. Y. Vul, M. Takahashi, M. Inakuma, M. Ozawa, E. Osawa. *Diamond Relat. Mater.* **14**, 1765 (2005).
16. N. Tagmatarchis, M. Prato. *Pure Appl. Chem.* **77**, 1675 (2005).
17. M. Califano, A. Zunger, A. Franceschetti. *Annu. Rev. Phys. Chem.* **52**, 193 (2001).
18. V. Klimov, A. Mikhailovsky, D. McBranch, C. Leatherdale, M. Bawendi. *Science* **287**, 1011 (2000).
19. R. D. Schaller, J. M. Pietryga, S. V. Goupalov, M. A. Petruska, S. A. Ivanov, V. I. Klimov. *Phys. Rev. Lett.* **95**, 196401 (2005).
20. A. Johnson, J. Petta, J. Taylor, A. Yacoby, M. Lukin, C. Marcus, M. Hanson, A. Gossard. *Nature* **435**, 925 (2005).
21. H. Htoon, M. J. O'Connell, S. K. Doorn, V. I. Klimov. *Phys. Rev. Lett.* **94**, 127403 (2005).
22. G. Lanzani, G. Cerullo, A. Gambetta, C. Manzoni, E. Menna, M. Meneghetti. *Synth. Met.* **155**, 246 (2005).
23. T. Hertel, G. Moos. *Phys. Rev. Lett.* **84**, 5002 (2000).
24. F. Wang, G. Dukovic, L. E. Brus, T. F. Heinz. *Phys. Rev. Lett.* **92**, 177401 (2004).
25. H. Kamisaka, S. V. Kilina, K. Yamashita, O. V. Prezhdo. *Nano Lett.* **6**, 2295 (2006).
26. C. D. Spataru, S. Ismail-Beigi, L. X. Benedict, S. G. Louie. *Phys. Rev. Lett.* **92**, 077402 (2004).
27. R. B. Capaz, C. D. Spataru, P. Tangney, M. L. Cohen, S. G. Louie. *Phys. Rev. Lett.* **94**, 036801 (2005).
28. I. A. Howard, D. J. Klein, N. H. March, C. V. Alsenoy, S. Suhai, Z. Janosvalfi, A. Nagy. *J. Phys. Chem. B* **108**, 14870 (2004).
29. Y.-C. Chen, N. R. Raravikar, L. S. Schadler, P. M. Ajayan, Y.-P. Zhao, T.-M. Lu, G.-C. Wang, X.-C. Zhang. *Appl. Phys. Lett.* **81**, 075 (2002).
30. B. J. LeRoy, S. G. Lemay, J. Kong, C. Dekker. *Nature* **432**, 371 (2004).
31. M. Oron-Carl, F. Hennrich, M. M. Kappes, H. V. Lohneysen, R. Krupke. *Nano Lett.* **5**, 1761 (2005).
32. F. W. Wise. *Acc. Chem. Res.* **33**, 773 (2000).
33. J. J. Peterson, T. D. Krauss. *Phys. Chem. Chem. Phys.* **8**, 3851 (2006).
34. P. Liljerothos, P. A. Z. van Emmichoven, S. G. Hickey, H. Weller, B. Grandidier, G. Allan, D. Vanmaekelbergh. *Phys. Rev. Lett.* **95**, 086801 (2005).
35. J. M. Harbold, H. Du, T. D. Krauss, K. S. Cho, C. B. Murray, F. W. Wise. *Phys. Rev. B* **72**, 195312 (2005).
36. Al. L. Efros, A. L. Efros. *Sov. Phys. Semicond.* **16**, 772 (1982).
37. L. E. Brus. *J. Chem. Phys.* **80**, 4403 (1984).
38. C. F. Craig, W. R. Duncan, O. V. Prezhdo. *Phys. Rev. Lett.* **95**, 163001 (2005).
39. J. C. Tully. *J. Chem. Phys.* **93**, 1061 (1990).
40. S. Hammes-Schiffer, J. C. Tully. *J. Chem. Phys.* **101**, 4657 (1994).
41. P. V. Parahdekar, J. C. Tully. *J. Chem. Phys.* **122**, 094102 (2005).
42. M. A. L. Marques, E. K. U. Gross. *Annu. Rev. Phys. Chem.* **55**, 427 (2004).

43. R. Baer, D. Neuhauser. *J. Chem. Phys*. **121**, 9803 (2004).
44. S. Tretiak, K. Igumenshchev, V. Chernyak. *Phys. Rev. B* **71**, 033201 (2005).
45. J. C. Tully. In *Classical and Quantum Dynamics in Condensed Phase Simulations*, B. J. Berne, G. Ciccotti, D. F. Coker (Eds.), pp. 489–514, World Scientific, Singapore (1998).
46. D. F. Coker. In *Computer Simulations in Chemical Physics*, M. P. Allen, D. J. Tildesley (Eds.), pp. 315–377, Kluwer Academic, Dordrecht (1993).
47. O. V. Prezhdo. *Theor. Chem. Acc.* **116**, 206 (2006).
48. J. P. Perdew. In *Electronic Structure of Solids*, P. Ziesche, H. Eschrig (Eds.), Akademie Verlag, Berlin (1991).
49. D. Nerukh, J. H. Frederick. *Chem. Phys. Lett*. **332**, 145 (2000).
50. F. Wang, G. Dukovic, L. E. Brus, T. F. Heinz. *Science* **308**, 838 (2005).
51. O. V. Prezhdo, P. J. Rossky. *Phys. Rev. Lett.* **81**, 5294 (1998).
52. A. Luis. *Phys. Rev. A* **67**, 062113 (2003).
53. G. Kresse, J. Furthmüller. *Comput. Mater. Sci.* **6**, 15 (1996).
54. D. Vanderbilt. *Phys. Rev. B* **41**, 7892 (1990).
55. K. P. Bohnen, R. Heid, H. J. Liu, C. T. Chan. *Phys. Rev. Lett.* **93**, 245501 (2004).
56. E. A. Albanesi, E. L. P. Y. Blanca, A. G. Petukhov. *Comput. Mater. Sci*. **32**, 85 (2005).
57. G. Allan, C. Delerue. *Phys. Rev. B* **70**, 245321 (2004).
58. W. H. Miller, T. F. George. *J. Chem. Phys*. **56**, 5637 (1972).
59. O. N. Kalugin, V. V. Chaban, Y. V. Kolesnik. *Russ. J. Phys. Chem.* **80**, 1273 (2006).
60. O. N. Kalugin, M. N. Volobuev, A. V. Ishchenko, A. K. Adya. *J. Mol. Liq.* **85**, 299 (2000).
61. D. Nerukh, T. R. Griffiths. *J. Mol. Liq.* **109**, 83 (2004).
62. P. Exner. *J. Phys. A: Math. Gen.* **38**, L449 (2005).
63. I. Kondov, U. Kleinekathofer, M. Schreiber. *J. Chem. Phys.* **119**, 6635 (2003).
64. V. Perebinos, J. Tersoff, P. Avouris. *Phys. Rev. Lett.* **94**, 027402 (2005).